

Hierarchical van der Waals Heterostructure Strategy to Form Stable Transition Metal Dichalcogenide Dispersions

Junmo Park,[§] Sungmin Bong,[§] Jaehyun Park, Eunji Lee,^{*} and Sang-Yong Ju^{*}Cite This: <https://doi.org/10.1021/acsami.2c12592>

Read Online

ACCESS |



Metrics & More



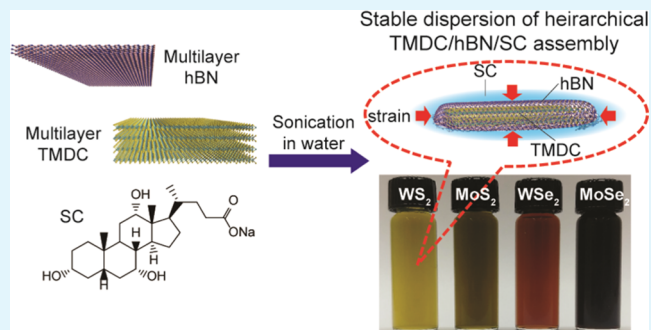
Article Recommendations



Supporting Information

ABSTRACT: Although various methods have been developed to disperse transition metal dichalcogenides (TMDCs) in aqueous environments, the methodology to generate stable TMDC dispersions remains challenging. Here, we developed a hierarchical van der Waals (vdW) heterostructure-based strategy to disperse few-layered TMDCs (WS_2 , MoS_2 , WSe_2 , and $MoSe_2$) using both hexagonal boron nitride (hBN) and sodium cholate (SC) as synergistic vdW surfactants. By showing long-term stability of up to 3 years, the extinction spectra of these TMDC/hBN/SC dispersions exhibit the most blue-shifted excitonic transitions, low background extinction, good colloidal stability, and dispersion stability upon ultracentrifugation compared to other dispersion methods. Hierarchical stacking having TMDCs and hBN/SC as core and shell parts is probed by electrostatic/atomic force microscopy and zeta potential, and its origin was attributed to surface energy matches. Along with the synergetic effect between TMDCs and hBN, the blue shift was ascribed to compressive strain on the TMDCs caused by hBN wrapping. The results of transmission electron microscopy show that the TMDCs in the dispersions have defective, few-layered structures with flake sizes that are less than a few hundred nm^2 . Raman spectroscopy is used to study not only the existence of compressive strain but also various interlayer coupling between TMDC and hBN. The hierarchical structures of TMDC/hBN/SC are discussed in terms of surface energies and topographies. This method is invaluable to provide a general methodology to disperse various surface-corrugated dimensional materials for various dispersion-based applications.

KEYWORDS: transition metal dichalcogenide, hexagonal boron nitride, dispersion, van der Waals heterostructure, hierarchical assembly, sodium cholate



INTRODUCTION

Transition metal dichalcogenides (TMDCs) have few-atom-thick hexagonal layered structures in which one layer composed of transition metal atoms (M) is sandwiched between two layers of chalcogen atoms (X). TMDCs comprised of different M and X atoms have a variety of different band gaps.¹ Monolayer TMDCs such as MoS_2 , $MoSe_2$, WS_2 , and WSe_2 possess direct band gap structures² that make them useful for optoelectronic applications including thin-film transistors,^{3–6} electrocatalysts,^{7,8} and spin-valley electronics.⁹ As a result, solution-processable and stable TMDC dispersions have broad applications.

Great effort has been made to develop methods to create processable and stable TMDC dispersions in various media. Studies targeted at this goal have led to several useful approaches including simple solvent,^{10,11} intercalation-assisted,^{12–15} and covalent^{16,17} and noncovalent^{18–20} based dispersion methods. TMDC dispersions^{10,11} formed using simple neat solvents have stabilities that intrinsically depend on surface energy differences where large differences result in unstable dispersions. The metal intercalation method^{12,13}

utilizes alkali metals to intercalate TMDCs in the form of alkali cation-coordinated TMDC solvent dispersions. Covalent dispersions mainly utilize the chemistry of thiol-terminated ligands^{16,17} such as lipoic acid to functionalize TMDCs. In contrast, noncovalent functionalization utilizes amphiphilic surfactants,^{18,19} which consist of hydrophilic and hydrophobic components, to interact with the respective aqueous and TMDC surfaces. However, a major hurdle confronting the employment of these approaches to create dispersions is associated with the atomically corrugated nature of TMDC surfaces, which causes an energetic barrier for solvation (or micellization) by solvent (surfactant) that negatively impacts stability.

Received: July 14, 2022

Accepted: October 17, 2022

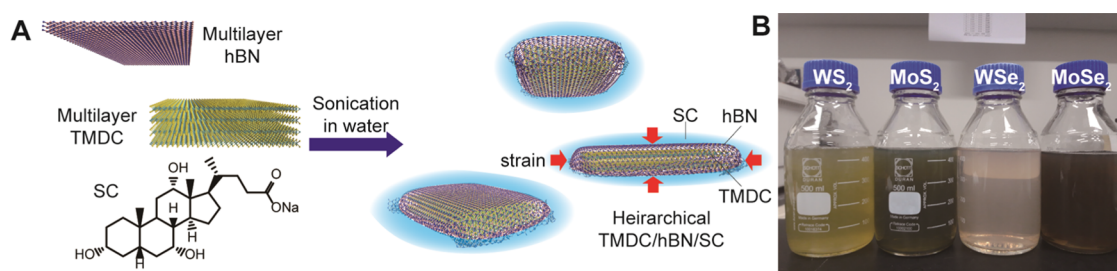


Figure 1. (A) Schematic of the vdW heterostructure strategy to disperse TMDCs in water using hBN and SC. SC provides anionic stability owing to the presence of a carboxylate group at the outmost exterior, and hBN serves as an interfacial layer between SC and the TMDC. Atomic color code: blue: nitrogen; purple: boron; yellow: sulfur; and green: molybdenum. (B) Photograph of large-scale TMDC dispersions obtained by centrifugation at 5 kg.

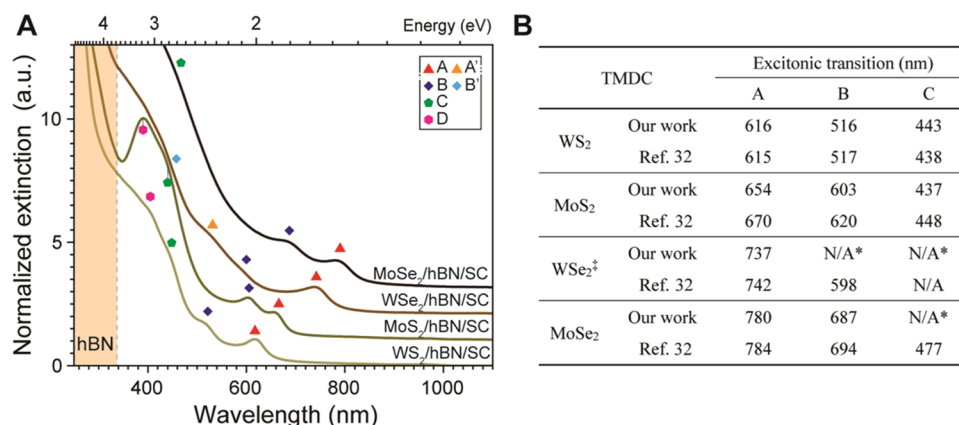


Figure 2. Optical characteristics of TMDC/hBN/SC dispersions. (A) Normalized offset UV–vis–NIR extinction spectra of TMDC dispersions obtained by centrifugation at 5 kg with hBN/SC against the A exciton. Offset is by 1. Excitonic transitions such as A, B, C, and D, along with A' and B' are denoted using different symbols and colors. (B) Excitonic transitions of TMDC/hBN/SC dispersions centrifuged at 5 kg centrifugal force along with those of CVD-grown TMDCs on the SiO₂/Si substrate. N/A: uncertainty exists due to peak broadening. [‡]In this spectral range, WSe₂ contains A' and B' transitions instead of C.

As a result, we have carried out investigations to explore a novel methodology to overcome disadvantages associated with current protocols. Specifically, we have assessed a new van der Waals (vdW) heterostructure-based strategy to disperse TMDCs (WS₂, MoS₂, WSe₂, and MoSe₂), which uses both hexagonal boron nitride (hBN) and sodium cholate (SC) as synergistic vdW surfactants. hBN possesses a wide direct band gap (6.0 eV),²¹ thermal stability (to 1300 °C),²² and distinguished chemical stability compared to graphene.^{23,24} Moreover, methods to disperse hBN, using commercially available surfactants such as sodium cholate (SC, see Figure 1A for the chemical structure)²⁵ and sodium dodecyl sulfate,²⁶ have been extensively studied. Because they possess hydrophobic faces, these types of amphiphilic surfactants²⁷ smoothly interface with the relatively hydrophobic hBN surface. Moreover, hBN serves as a dielectric layer in TMDC thin-film transistors, where it minimizes the interaction between the TMDCs and the SiO₂/Si substrate because of the strong vdW interaction.⁶ Especially when utilized as a bottom or top layer in fabrication of these devices via the deterministic transfer method,^{5,6} hBN provides a charge-inert environment for TMDCs by screening charge inhomogeneity, leading to high carrier mobility and performance. Moreover, the occurrence of vdW interactions between MoS₂ and hBN has been documented by the observation of higher frequency shifts of the out-of-plane Raman mode of MoS₂ sandwiched between hBN²⁸ and Raman spectrum changes of graphene/TMDC heterostructures as well.²⁹

In the investigation described below, we demonstrate that a vdW surfactant combination consisting of hBN and SC (hBN/SC) serves as a synergistic hierarchical dispersing agent to prepare stable dispersions of MoS₂, MoSe₂, WS₂, and WSe₂ in water. Importantly, the results show that the vdW surfactant interacts with the TMDCs not only to enable dispersion formation but also to cause dramatic blue shifts of excitonic transitions along with low backgrounds in extinction spectra. The hierarchical structure having TMDC/hBN/SC is probed by electrostatic force microscopy (EFM) and atomic force microscopy (AFM). The excitonic blue shifts originate from the presence of compressive biaxial strain on the TMDCs when they are wrapped by hBN. The stabilities of the vdW surfactant-promoted TMDC dispersions were probed by the zeta (ζ) potential method. Transmission electron microscopy (TEM) was also utilized to show that the dispersions consist of few-layered TMDCs. Finally, Raman spectroscopy was employed to probe the effects of compressive wrapping and interlayer coupling on TMDCs exerted by hBN.

RESULTS AND DISCUSSION

A schematic illustrating a new method to produce TMDCs wrapped by hBN and SC is shown in Figure 1A. In the process, a dispersion creates a hierarchical structure of hBN-wrapped TMDC (MoS₂, MoSe₂, WS₂, or WSe₂) to form a vdW heterostructure and then by SC acting as an anionic surfactant between the vdW heterostructure and aqueous medium. By providing a vdW heterostructure, hBN lowers the surface

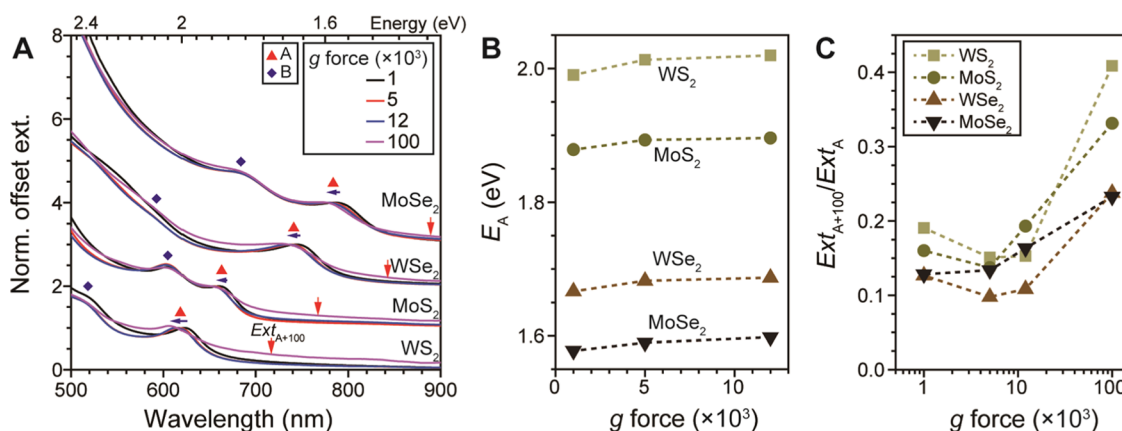


Figure 3. Effect of varying centrifugal forces on the extinction spectra and A positions of TMDC/hBN/SC dispersions. (A) Normalized offset extinction spectra of TMDC/hBN/SC dispersions with increasing centrifugal forces. Normalization was conducted against each A transition, and offset was by 1 extinction. Red arrows indicate reference points for the background extinction (that is, Ext_{A+100}). (B) E_A according to increasing centrifugation force. (C) Ratio of Ext_{A+100} over Ext_A according to centrifugation force.

energy barrier of the TMDC, while SC, located in the outermost layer at the interface between water and hBN, provides anionic repulsion for the vdW heterostructure so that it is stably dispersed.

The relative weight ratio of TMDC and hBN to form efficient dispersions was determined by considering the surface areas of each monolayer. Based on the hexagonal lattice of MoS₂ ($a = 3.12 \text{ \AA}$) and hBN ($a = 2.50 \text{ \AA}$), the respective surface areas of monolayers are *ca.* 634 and 2626 m²/g, indicating that the weight per unit area of MoS₂ should be 2.6 times greater than that of hBN. To create the wrapped TMDC structure by hBN on both sides, a mixture of TMDC (10 mg) and hBN (2 mg) was mixed with water (4 mL) containing 1 wt % SC, which exceeds its critical micelle concentration (15 mM).^{30,31} The mixture was subjected to brief bath sonication for sample homogenization, and long tip sonication for TMDC exfoliation (see the [Experimental Section](#)). Centrifugation was then conducted at varying centrifugal forces (1, 5, 12, and 100 kg, *g*: gravitational acceleration speed), giving 80% of the supernatant that was subjected to subsequent measurements.

Modification of the sonication method from tip to cup-horn sonication allows dispersing large-scale exfoliated of TMDC/hBN/SC, as shown in [Figure 1B](#). The photograph of representative TMDC/hBN/SC dispersions shows that they display dense and distinct colors that correspond to the individual TMDC components (yellow, green, red, and brown for WS₂, MoS₂, WSe₂, and MoSe₂ dispersions, respectively). A consideration of the relatively higher centrifugation conditions (i.e., a few thousands of *g*) used for TMDC/hBN/SC dispersions compared to those needed for other surfactant-based counterparts (i.e., lower centrifugal conditions such as a few hundreds of *g*)^{18,19} suggests that these dispersions prepared using the vdW surfactant are quite stable.

The extinction spectra of TMDC/hBN/SC display the blue-shifted optical transitions and lower background extinction. UV–vis–near IR (NIR) extinction spectra acquired using TMDC/hBN/SC dispersions prepared with 5 kg centrifugation ([Figure 2A](#)) are displayed in a normalized offset manner according to the increasing wavelength of A transition (λ_A), which is the lowest-lying excitonic transition of semiconducting 2H TMDCs.^{2,17,32} By virtue of transparent hBN and SC whose absorption tail vanishes at 350 nm, distinct excitonic transitions A, B, and C with increasing wavelengths can be seen

in these spectra, as listed in [Figure 2B](#). λ_A increases in the order 616, 654, 737, and 780 nm for WS₂, MoS₂, WSe₂, and MoSe₂, respectively. Similarly, λ_B increases in the order 516, 603, and 687 nm for WS₂, MoS₂, and MoSe₂, respectively, except for WSe₂ whose λ_B has uncertainty originating from broadening. Overall, MoSe₂ displays the smallest band gap (E_g) among the TMDCs. Especially, the energy between A and B transitions is the smallest from Mo-derived TMDCs. The reason for this trend originates from the band gap structure in hybridization of the d orbital of transition metals (Mo and W) with the p orbital of chalcogens (S and Se) and in good agreement with 2H semiconducting TMDCs from theoretical³³ and experimental³⁴ results. Unlike other TMDC dispersions, the optical transitions of dispersed WSe₂ are strongly affected by Se p orbitals,³⁴ causing the occurrence of additional A' and B' transitions in the high-energy region.^{34,35} These transitions of dispersions centrifuged at 5 kg are compared with those of CVD-grown TMDCs on a SiO₂/Si substrate³² ([Figure 2B](#)). The spectrum of MoS₂, a representative TMDC, contains A, B, and C transitions at 654, 603, and 437 nm, respectively, which are all blue-shifted from those of CVD-grown MoS₂. This trend is true for comparison with other dispersions as well: energy of A (E_A) is blue-shifted by 37 and 23 meV for covalently functionalized MoS₂ in water by lipoic acid^{16,17} and few-layered MoS₂/SC dispersion isolated using density gradient centrifugation,¹⁹ respectively. Moreover, the MoS₂/hBN/SC dispersion contains the most blue-shifted transitions among those of MoS₂ dispersed in various solvents.³⁶

The increasing centrifugal force during preparation induces a further blue shift of A transitions, reduction of the resulting extinction from TMDC/hBN/SC dispersion, and reduction in TMDC concentration. By inspecting the normalized extinction spectra displayed in [Figure 3A](#), we observed that increasing *g* (1, 5, 12, and 100 kg) leads to a progressively large blue shift of A excitonic transitions. A transition of other TMDCs also blue shifts with increasing *g* ([Figure 3B](#)). These changes accompany reductions in TMDC concentrations ([Figure S1A–D](#) and their insets for their extinction spectra and trend). Specifically, the E_A values of the dispersions generated from MoS₂, MoSe₂, WS₂, and WSe₂ prepared at 12 kg are blue-shifted by 29, 17, 20, and 20 meV from those of 1 kg-centrifuged dispersions. Although further blue shifts occur in TMDC dispersions

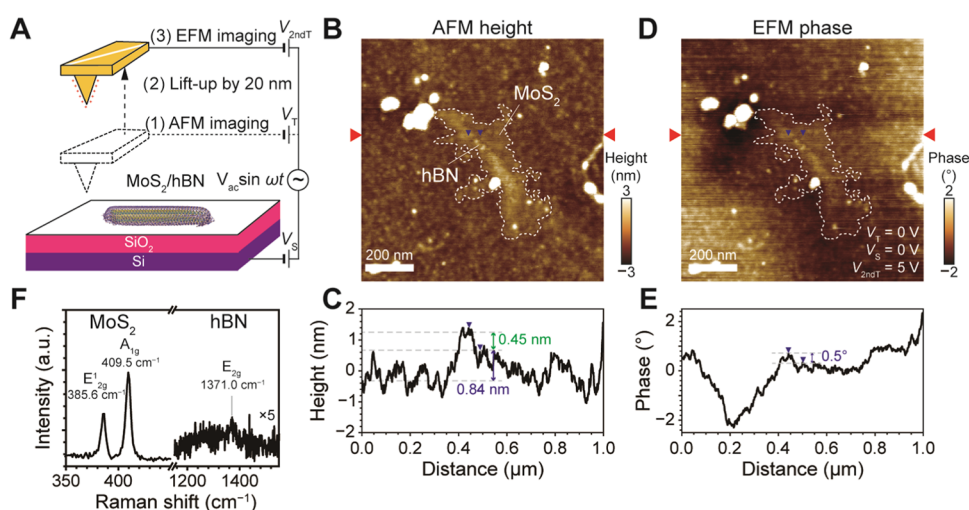


Figure 4. Hierarchical structure of the MoS₂/hBN/SC structure probed by EFM. (A) Schematic for EFM measurements. (B) AFM height image acquired by tapping mode and (C) height profile along the line in the facing triangles of (B). The 12 kg-processed MoS₂/hBN/SC sample was deposited on a 285 nm thick SiO₂/Si substrate and was subjected to washing with a copious amount of water. (D) Corresponding EFM phase image and (E) phase profile acquired by lifting up the tip under the following conditions: $V_S = 0$ V, $V_T = 0$, and $V_{2ndT} = 5$ V. (F) Raman spectrum of the sample.

prepared using 100 kg, wavelength uncertainty exists because of significant peak broadening.

Another point worth discussing is related to the observation that the extinction spectra (Figure 3A) exhibit the smallest background extinction at intermediate centrifugal forces from 5 to 12 kg. Typically, solvent- or surfactant-exfoliated TMDCs exhibit larger background extinction owing to the large flake bundles and thickness.^{10,11,19} For this, the ratio of extinction at a wavelength 100 nm greater than that of A transitions (Ext_{A+100} , dashed line) over extinction of A (Ext_A) was used to quantify the background contribution in each spectrum, as shown in Figure 3C. The minimal values for background extinction were found to be near 5 to 12 kg centrifugation conditions irrespective of TMDC type. The initially decreased ratio indicates the sorting to few-layered TMDCs due to high centrifugal force, according to the literature.¹⁸ However, further increased g force results in an increased ratio. Judging by normalized extinction in the valley between A and B transitions (Figure S2), such an increased ratio results from both reduced A transition and increased background extinction. Reduction of A transition seems to originate from defects whose dangling bonds might induce further buoyancy of defective TMDCs. Increased background extinction is attributed to partial delamination of hBN at higher centrifugal force.

These TMDC/hBN/SC dispersions exhibit excellent stability of up to 3 years. Figure S3A displays the offset extinction spectra of the as-dispersed and 3-year-old TMDC/hBN/SC samples prepared at 12 kg. Although slight broadening occurs, the TMDC spectra do not change dispersion significantly except for the WS₂ case for unknown reasons. Figure S3B displays the percentile ratio of extinction of A from the as-dispersed ($Ext_{A,as-dispersed}$) over extinction of A from the aged sample ($Ext_{A,aged}$). Clearly, 12 kg samples exhibit high stability over 50% retainment, whereas dispersions at 5 kg display lower values. The 100 kg TMDC sample displays intermediate retainment presumably due to the aforementioned delamination. The reason for the retainment of over 100% originates from natural evaporation of dispersing media.

Moreover, A excitation shifts (Figure S3C) obtained from A for the as-dispersed ($E_{A,as-dispersed}$) subtracted by the aged ($E_{A,aged}$) display at most a red shift of 7 meV according to g forces. These shifts are much less than those created by different centrifugation forces. This result clearly demonstrated the stability of TMDC/hBN/SC dispersions. In addition, consideration of the dielectric constant (ϵ) of monolayer hBN (3.29 and 6.82 for static out-of-plane and in-plane ϵ 's, respectively)³⁷ suggests that compressive strain rather than solvatochromism³⁶ is the main source of the observed blue shifts of the TMDC/hBN/SC dispersions (see the SI for a detailed discussion). Thus, increasing centrifugal force from 1 to 12 kg increases compressive biaxial strain by 0.17–0.29%. The excitonic position shifts do not occur in the spectra of TMDC dispersion prepared only using SC.¹⁸

The proposed hierarchical structure was confirmed by EFM.^{38,39} Since MoS₂ and hBN are a semiconductor and an insulator, respectively, they have different responses to the external electric field. EFM along with AFM enables us to discover that few-layered MoS₂ is covered by hBN. While AFM tapping mode is driven by vdW interaction with the sample, as shown in Figure 4A, EFM phase imaging is operated with a biased tip-sample with a larger height (typically >10 nm to exclude vdW interaction). The EFM phase image can record the capacitance of a sample surface by detecting the electrostatic force lagging due to the Coulombic interaction between the sample (V_S) and a biased AFM tip (V_{2ndT}). During the scan of the sample surface, the presence of electrostatic forces leads to a change in the oscillation amplitude and phase in the vertical deflection signal (see the SI for a detailed explanation). Figure 4B shows the AFM height image of MoS₂/hBN/SC deposited on 285 nm thick SiO₂/Si and subsequent washing with copious amounts of water to remove SC. The topography indicates that corrugated and irregular-shaped MoS₂ is situated on top of the 285 nm thick SiO₂/Si substrate. The topography (Figure 4C) indicates that the layer has a thickness of monolayer MoS₂ and, moreover, it has an additional partial 0.45 nm thick layer, corresponding to monolayer hBN. The corresponding EFM

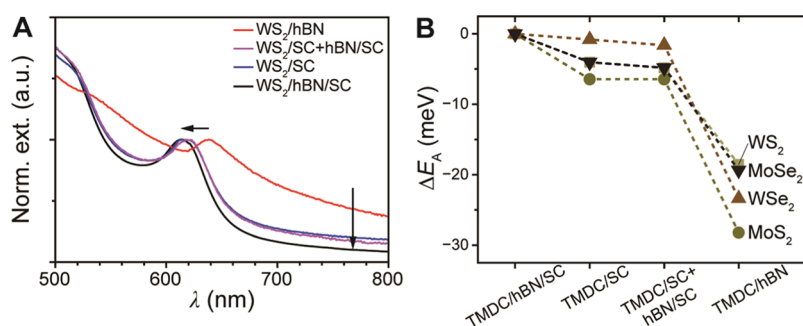


Figure 5. Effect of each constituent on TMDC dispersions prepared in the presence of hBN or SC, along with a 1:1 vol mixture of hBN/SC and TMDC/SC. The samples were prepared by 12 kg. (A) Normalized extinction spectra of various TMDC dispersions against the A exciton. (B) ΔE_A of TMDC dispersions with varying components against TMDC/SC/hBN dispersion.

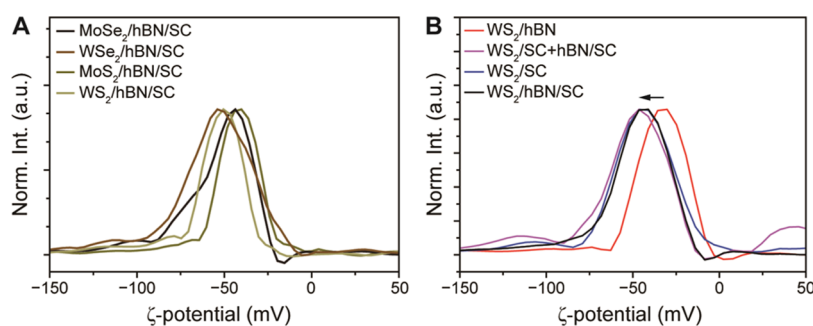


Figure 6. ζ -potential profiles of (A) WS_2 , MoS_2 , WSe_2 , and $MoSe_2$ dispersions assisted by hBN/SC centrifuged at 5 kg. (B) Effect of each constituent for WS_2 dispersions prepared in the presence of hBN or SC, along with an isovolume mixture of WS_2/SC and hBN/SC dispersions. Samples are prepared by 12 kg.

phase image (Figure 4D) and phase profile (Figure 4E) reveal that MoS_2 results in a large phase shift up to -2° due to the capacitance of its semiconducting nature, whereas hBN does not show an appreciable shift. Moreover, the Raman spectrum of this sample (Figure 4F) shows that it has vibrational features originating from both MoS_2 and hBN. The low-frequency region contains two bands at 385.6 and 409.5 cm^{-1} , which correspond to the E_{2g}^1 and A_{1g} modes of MoS_2 , respectively. The interpeak separation is 23.9 cm^{-1} . Moreover, the Raman active E_{2g} band of hBN^{40,41} appears at ~ 1371 cm^{-1} with an intensity that is much weaker than that of MoS_2 due to the nonresonant Raman condition (532 nm).

Cross-sectional TEM shows good interfacial MoS_2/hBN interaction without the SC adsorbate. For this, after the sample position was predetermined by the optical microscopy (OM) image, focused ion beam (FIB)-scanning electron microscopy (SEM) was utilized to prepare a lamella sample on the 285 nm thick SiO_2/Si substrate (see the Experimental Section and Figure S4A–C for the process). The resulting cross-sectional TEM (Figure S5A) shows multilayer hBN stacked on multilayer MoS_2 in which layer spacings of each material are ca. 0.35 and 0.65 nm, respectively. Moreover, the interface between MoS_2/hBN is clean without SC adsorbates. Its energy-dispersive spectroscopy (EDS) images (Figure S5B–C) confirm the localization of each atom (N, Mo, and S) in each layer according to the location, except for B whose lower binding energy of the boron K edge is situated at ca. 0.2 keV close to background signals. Additional TEM measurement of different areas (Figure S5D–F) also displays similar results.

The synergistic effect of TMDC/hBN/SC was investigated by performing a comparison with several control experiments that are dispersion preparation of TMDC/hBN and TMDC/

SC and a 1:1 vol mixture of hBN/SC and TMDC/SC dispersions in similar preparation conditions (i.e., 12 kg centrifugation). Figure 5A displays the resulting extinction spectra of each dispersion. Among those, $WS_2/hBN/SC$ dispersion displays the most blue-shifted λ_A and the smallest background extinction. The extinction spectrum of hBN/ WS_2 exhibits broad and less-featured spectra extended to the NIR region, suggesting poor dispersion due to larger bundling. In the case of WS_2/SC , the dispersion displays greatly reduced background extinction and a larger blue shift, similar to the case of a mixture of hBN/SC and TMDC/SC dispersions. Extinction spectra from other dispersions (Figure S4A–C) exhibit similar λ_A trends as well. Figure 5B displays the energy difference in A (ΔE_A) of various dispersions with respect to E_A from the TMDC/SC/hBN dispersion. A transition of the TMDC/hBN/SC dispersion exhibits the largest blue shift (from 17 to 28 meV) among dispersions. Especially, a mixture of TMDC/SC and hBN/SC dispersions was not able to achieve the blue shift of the A exciton and lower background extinction as much as those of TMDC/hBN/SC, suggesting a synergistic effect between TMDC and hBN in the presence of SC. The trend clearly indicates that the vdW interaction between hBN and TMDC is the main reason for the observed blue shift and stabilized dispersions.

To gain an understanding of the origin of stability, dispersions prepared using 5 kg centrifugation are subjected to ζ -potential measurements (Figure 6A). The maximum positions of each histogram correspond to surface charges that are less than -40 mV, indicating the anionic nature of the colloid. Typically, colloidal dispersions are stable when the absolute values of the ζ -potentials are greater than 30 mV irrespective of surface charge.⁴² Moreover, the ζ -potentials

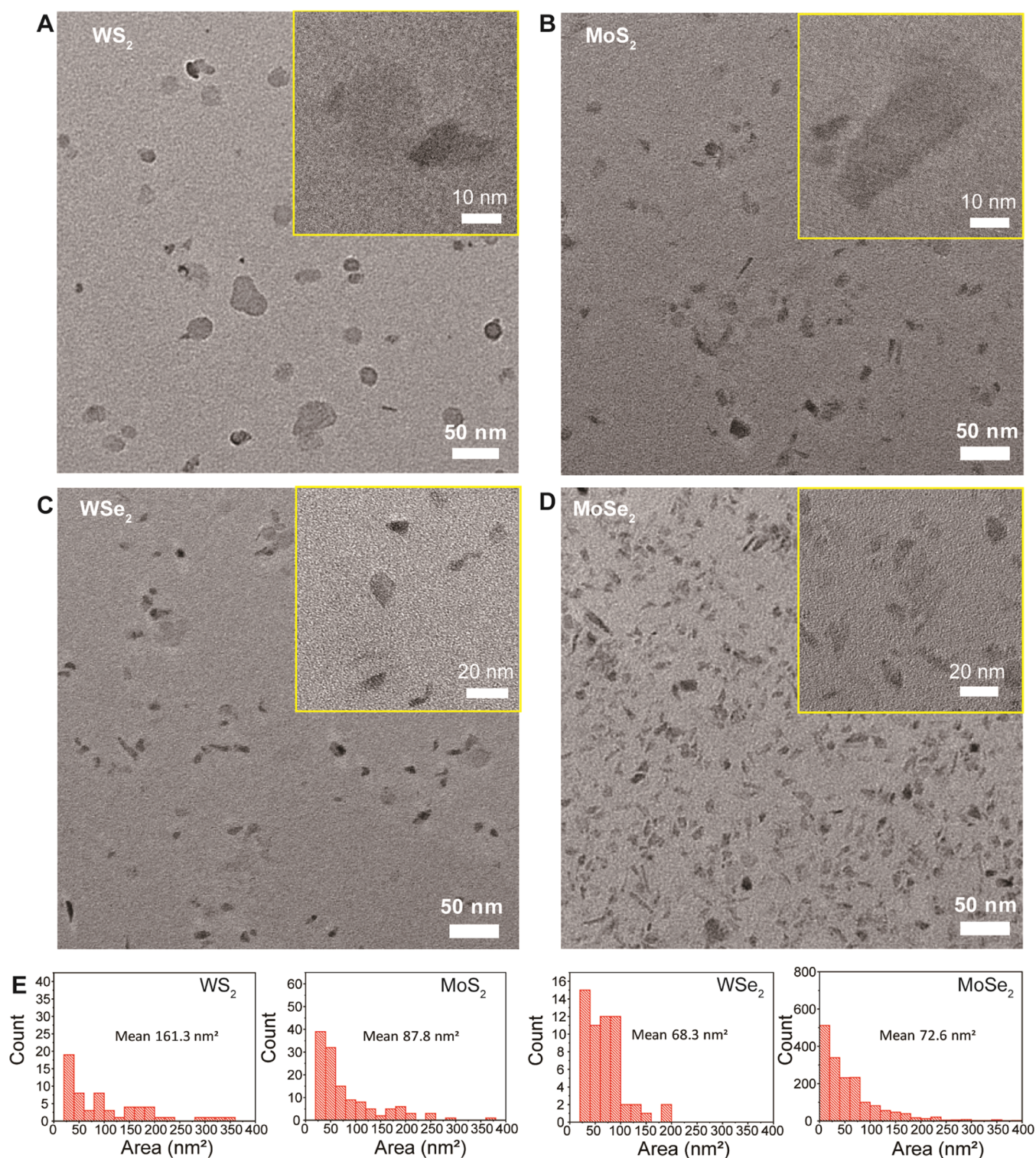


Figure 7. Size distributions of the TMDC/hBN/SC dispersions. TEM images of (A) WS₂, (B) MoS₂, (C) WSe₂, and (D) MoSe₂. Inset: corresponding more highly magnified images. (E) Resulting size histograms and mean values of the TMDC particles.

increase in the series from WSe₂, WS₂, MoSe₂ to MoS₂ with respective values of -52.0 , -50.7 , -46.6 , and -41.4 mV. This result suggests that SC, which contains an anionic carboxylate terminal, is the main reason for dispersion stability. Moreover, when the amounts of SC and hBN are held constant, the ζ -potentials of the W-based TMDC dispersions are slightly more negative. The ζ -potential, which is the potential of the outer diffuse layer in the electrical double layer,⁴² is dependent on

the pH of the solution and electrolyte concentration. Increasing pH leads to the build-up of a more negative charge on particles. The measured pH values of the as-prepared WSe₂, WS₂, MoSe₂, and MoS₂ dispersions were observed to be 7.10, 7.08, 7.06, and 6.91, respectively, which are in line with the observed ζ -potential trends. Similar measurements were conducted for control samples as well, as shown in Figure 6B. While WS₂/hBN displays a ζ -potential of -28.79 mV,

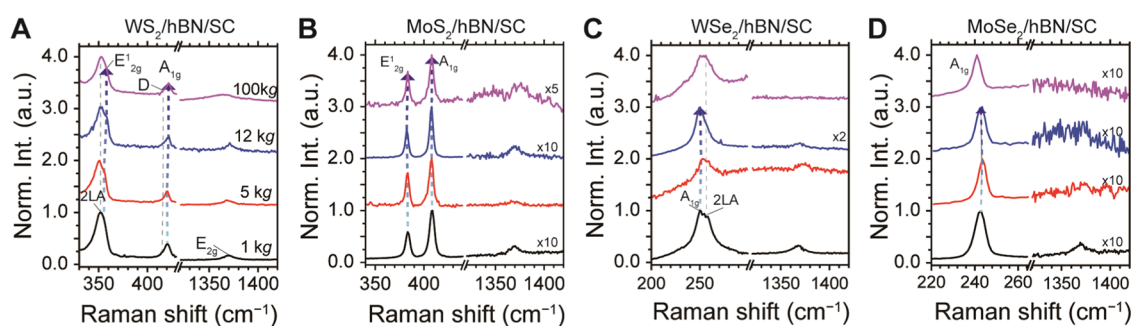


Figure 8. Normalized Raman spectra of (A) $\text{WS}_2/\text{hBN}/\text{SC}$, (B) $\text{MoS}_2/\text{hBN}/\text{SC}$, (C) $\text{WSe}_2/\text{hBN}/\text{SC}$, and (D) $\text{MoSe}_2/\text{hBN}/\text{SC}$ prepared using increasing centrifugal force and deposited on substrates. Excitation laser: 532 nm. Spectra in each group are offset by a 1.0 normalized intensity unit.

which exceeds the stable colloidal regime, other samples from WS_2/SC , isovolume mixture of $\text{WS}_2/\text{SC} + \text{hBN}/\text{SC}$, and $\text{WS}_2/\text{hBN}/\text{SC}$ dispersions show ζ -potentials at -40.17 , -43.54 , and -43.75 mV, respectively. This clearly indicates that SC is the major contributor to stability.

The colloid size distributions of TMDC/hBN/SC dispersions were determined by TEM. Figure 7A–D shows TMDC platelets on holey lacey carbon grids. Regardless of type, the TMDCs exhibit uniform plate-like structures with thin contrasts. The platelets have slightly different contrasts, indicating the existence of mixtures of few-layered TMDCs or hBN. Close-up TEM images (insets of Figure 7A–D) show that crystalline lattices are not present in the TMDC flakes, indicating defective TMDCs. The analysis of TMDC flakes by histogram distributions (Figure 7E) shows that most have lognormal distributions and that among four different TMDCs, WS_2 contains the largest flakes with an average size of 160 nm^2 . The remaining MoS_2 , WSe_2 , and MoSe_2 flakes have respective sizes of 88, 68, and 73 nm^2 .

Raman spectroscopy carried out using a 532 nm excitation laser was utilized to probe the compressive effect of hBN on TMDCs and its centrifugal force dependence. The dispersions were drop cast on 285 nm thick SiO_2/Si substrates and were washed with copious water to eliminate SC. First, the WS_2 dispersion generated by 1 kg centrifugation (Figure 8A) exhibits two prominent peaks at ~ 352 and $\sim 420 \text{ cm}^{-1}$. While the bands centered at $\sim 420 \text{ cm}^{-1}$ are assigned to out-of-plane A_{1g} modes of WS_2 , the $\sim 352 \text{ cm}^{-1}$ band consists of a major 2 longitudinal acoustic (2LA) band near the M point in the Brillouin zone and a minor in-plane E_{2g}^1 band.^{35,43} The E_{2g}^1 and A_{1g} bands from the sample processed by increasing g force are increasingly blue-shifted by 0.7 and 1.4 cm^{-1} , respectively, without a great change occurring in interpeak separation ($\sim 69 \text{ cm}^{-1}$). This behavior is also observed in the spectra of stacked WS_2/MoS_2 vdW heterostructures under compressive strain.⁴⁴ In addition, the 20 cm^{-1} band contains a shoulder along with the A_{1g} band, especially for a 100 kg prepared sample. The shoulder, which originates from the defect-related D band,⁴⁵ increases with increasing g , suggesting that more defective TMDCs are produced using higher g .⁴³ Moreover, the E_{2g}^1 band of hBN appears at $\sim 1370 \text{ cm}^{-1}$ with an intensity that is much weaker than that of WS_2 due to the nonresonant Raman condition.

Overall, the results show that WS_2 exhibits more compressive strain as g increases. It is noteworthy that the interpeak separation does not match those of few-layered TMDCs, and therefore, it might originate from interactions between hBN and WS_2 . In this regard, when MoS_2 is

encapsulated between hBN, the E_{2g}^1 and Raman A_{1g} modes²⁸ of monolayer MoS_2 are downshifted and upshifted by 1 and 2 cm^{-1} , respectively, and the E_{2g}^1 band of multilayer MoS_2 is downshifted by $2\text{--}3 \text{ cm}^{-1}$.

The Raman spectrum of $\text{MoS}_2/\text{hBN}/\text{SC}$ dispersion prepared at 1 kg (Figure 8B) contains two bands at 383.5 and 408.3 cm^{-1} , which correspond to E_{2g}^1 and A_{1g} modes of MoS_2 , respectively. The interpeak separation of 1 kg is 24.8 cm^{-1} and decreases slightly (i.e., 24.5 cm^{-1}) when the dispersion is generated at higher g levels. The 383.5 and 408.3 cm^{-1} bands display blue shifts upon increasing g . The Raman spectrum of the WSe_2 dispersion (Figure 8C) contains a band at 250.0 cm^{-1} originating from the A_{1g} mode. However, like WS_2 , a band for the 2LA mode overlies the right shoulder. This observation is in good agreement with that (250 cm^{-1}) made for multilayer WSe_2 .^{35,46} Moreover, the hBN band in the 100 kg sample disappears at higher centrifugal force, suggesting that less interaction exists between WSe_2 and hBN for a currently unknown reason. Lastly, the Raman spectrum of MoSe_2 dispersion (Figure 8D) contains a peak at 242.5 cm^{-1} corresponding to the A_{1g} mode of MoSe_2 .^{42,47} Upon increasing centrifugal force, the band exhibits a slight blue shift. The spectrum of the dispersion prepared at 100 kg without hBN has an A_{1g} band that is red-shifted by 1.5 cm^{-1} , which approaches that of few-layered MoSe_2 . This behavior might be a consequence of the occurrence of delamination of hBN from the TMDC dispersion, which is observed from the extinction spectrum at higher centrifugal force. Nevertheless, this result clearly suggests that the TMDC in the presence of hBN exhibits in a spectral up-frequency shift of the A_{1g} mode.

Interestingly, interlayer coupling mode between TMDC and hBN, photoluminescence, and overtone can be observed in the intermediate frequency region. Figure S5A–D shows Raman spectra of intermediate frequency regions from 700 to 1300 cm^{-1} . In this region, the out-of-plane optical (ZO) mode of hBN can be observed at around 820 cm^{-1} (Figure S5A–D). Interestingly, this mode is coupled with the E_{2g}^1 mode of WS_2 (top trace of Figure S5A), showing the 1170 cm^{-1} band. These interlayer-coupled vibrational modes have been observed before.⁴⁷ On top of these, we can observe broad photoluminescence originating from the B exciton of WS_2 . These regions also contain strong overtones of E_{2g}^1 , A_{1g} , and a combination of A_{1g} and E_{2g}^1 from the $\text{MoS}_2/\text{hBN}/\text{SC}$ sample, as shown in Figure S5B. The lack of these features in other samples suggests that these overtone and combination bands originate from the resonance Raman effect resulting from a partial overlap with the B transition of MoS_2 with an excitation

laser. Overall, TMDC/hBN/SC provides ample vibrational modes in conjunction with a heterostructure.

The driving force for the hierarchical assembly of TMDC/hBN/SC dispersions is attributed to surface energy match. The surface energy of water is approximately 72.8 mN/m (ref 48), whereas those of hBN (ref 49), MoS₂ (ref 50), and WS₂ (ref 51) are 72.1, 46.5, and 39 mN/m, respectively, and those of other TMDCs are not available. Therefore, these stepwise surface energy differences promote hierarchical stacking (i.e., TMDC/hBN/SC in water) of the heterostructure. On the other hand, the interface with larger surface energy differences between hBN and TMDC is expected to have less interaction because such a large difference favors cohesion rather than adhesion at the interface. This might explain the smaller blue shift of WS₂ in the WS₂/hBN/SC heterostructure compared to that of MoS₂/hBN/SC. Moreover, the hydrophobic face of SC is expected to be better associated with atomically flat hBN rather than the corrugated TMDC surface.

CONCLUSIONS

In the study described above, we have developed a vdW heterostructure-based strategy to prepare stable TMDC (WS₂, MoS₂, WSe₂, and MoSe₂)/hBN/SC dispersions in which hBN and SC serve as vdW surfactants. In the dispersions, hBN serves as an efficient interfacial two-dimensional material and SC provides anionic stabilization. By showing long-term stability of up to 3 years, extinction spectra of dispersions containing TMDCs wrapped by hBN/SC display large blue-shifted excitonic transitions and lower background extinction and are stable up to 100 kg centrifugation. Compared to those of other dispersed and CVD-grown TMDCs, the blue shift of the A transition, which increases at higher centrifugation force, originates from compressive biaxial strain exerted by hBN wrapping, which is observed in extinction and Raman spectroscopies. A hierarchical structure composed of TMDC/hBN/SC was confirmed by EFM, which differentiates the capacitance of TMDCs and hBN. Along with control experiments, the dispersion stability originates from the presence of anionic sodium carboxylate of SC organized on the vdW heterostructure dispersion, as evidenced by ζ -potentials greater than -40 mV. TEM analysis revealed that TMDCs in the dispersions consist of defective, few-layered TMDCs with average sizes below 160 nm². Raman spectra of these dispersions contain vibrational modes associated with not only the compressive strain of the TMDCs by hBN but also interlayer coupling, overtone, and photoluminescence in the intermediate frequency region. The driving force for the hierarchical vdW structure was attributed to surface energy matching. The ability to produce hierarchical TMDC/hBN/SC dispersions in a facile and highly stable manner suggests that the novel method will be useful in optoelectronic applications as well as sensory schemes based on dispersions.

EXPERIMENTAL SECTION

Materials and Instrumentation. WS₂ (powder form, >99.8% purity, Lot. no.: #Q21C048), WSe₂ (micron powder form, >99.8%, 10–20 μ m, Lot. no.: #P06E002), and MoSe₂ (mesh powder form, >99.9%, mesh size = 325 (<40 μ m), Lot. no.: #T16E048) were purchased from Alfa Aesar. MoS₂ (powder form, >99%, <2 μ m, Lot. no.: #1371634V) and hBN (>98%, \sim 1 μ m, Lot. no.: #STBH5311) were purchased from Merck. Sodium cholate salt (>98% purity, Lot. no.: #XMSVL-AB) was purchased from TCI. UV–vis–NIR extinction spectra were recorded on a spectrophotometer (V-770, JASCO,

Japan) with absorption cuvettes having a 10 mm beam path (Lot. no.: 100–10–40, QS, Hellma Analytics, Germany) or a 1 mm path length (21/Q/1, Starna scientific, U.K.) unless otherwise noted. Extinctions were measured via a double beam configuration. The ζ -potential was measured by an ELS-1000ZS (Otsuka Electronics, Japan). The pH of dispersions was acquired by a SevenMulti pH meter (Mettler Toledo), which was calibrated with three known buffered pH references (i.e., 4.01, 7.00, and 10.01) prior to measurement.

TMDC Dispersions. The dispersion ratio for TMDC/hBN/SC/DI water was 10 mg:2 mg:40 mg:4 mL, respectively, and the typical dispersion volume was 40 mL, which was subjected to sonication. The resulting mixture was subjected to 10 min bath sonication (5 min, Branson 1510, 70 W, Emerson, MO) for initial homogenization and further 2 h tip sonication [40% power, 18.8 W/mL, probe tip diameter: 13 mm, VCX 750, Sonics & Materials, CT] during which the resonator was cooled with an external air cooler. During sonication, the temperature of the sample vials was maintained at 20 °C by an external water circulator (RW-2025G, Lab Companion, Republic of Korea). Large aggregates were discarded for 1, 5, and 12 kg with a benchtop centrifugator (Wisepin CF-10, Woongkiscience) or 100 kg with an ultracentrifugator (Optima Max-up, Beckman Coulter). The 80% supernatant was carefully collected for subsequent measurements. Control dispersions (i.e., TMDC/hBN, TMDC/SC and a 1:1 mixture of hBN/SC and TMDC/SC) were prepared with a maintained wt. ratio to water as that of TMDC/hBN/SC dispersions. Centrifugation was performed in a similar manner as well. For large-scale exfoliation, the cup-horn sonication method was utilized. Three 40 mL vials containing the TMDC/hBN/SC mixture in water were subjected to sonication for 2 h. Then, 5 kg centrifugation was applied and 80% of the supernatant was utilized for the measurement. A similar protocol mentioned above was applied unless otherwise noted.

Raman Measurement. Micro Raman measurements were conducted using a custom-made instrument equipped with a 532 nm laser (Cobolt 08-DPL, Hubner Photonics) via a backscattering geometry according to the previous literature.^{52–55} Briefly, inelastic scattering signals from the focused laser spot on the sample were collected via an objective lens (50 \times or 100 \times , Plan, Olympus, Japan) in an upright microscope (BX51, Olympus, Japan). The collected scattering was focused via a tube lens in a trinocular of the microscope and dispersed and recorded with a spectrometer (Triax320, Horiba, Japan) with 1800 g/mm (resolution < 1 cm⁻¹) and a charge-coupled device detector (Synergy, Horiba, Japan). Measurements were conducted from a drop cast sample on a 285 nm thick SiO₂/Si substrate with 0.1 mW for 300 or 500 s and utilized the 520.89 cm⁻¹ Si peak as an internal reference.

AFM and EFM Measurements. The measurement was performed by an NX10 (Park systems, Republic of Korea). A Au-coated conductive tip (PPP-NCSTAu-10, Au coated on both sides) was utilized to obtain both AFM and EFM images. For the EFM measurement, as shown in Figure 3, the sample deposited on a conductive disk was biased with $V_s = 0$ V and $V_t = 0$ V. This mode is operated in tapping mode. Upon lift-up by 20 nm from the highest height, a tip voltage (V_{2ndT}) of 5 V was applied. Typically, 512 pixel \times 512 pixel images were acquired.

TEM Measurements. TEM images were recorded using a JEM-3011 HR and a JEM-2100 (JEOL, Japan). Copper TEM grids covered with an ultrathin carbon support film on a lacey carbon support (LC200-CU, Lot. no.: 180912, 200 mesh, Electron Microscopy Sciences) were used. The TMDC dispersion sample was drop cast on the TEM grid and diluted by DI water about 5 times. For cross-sectional TEM measurement, the sample on the 285 nm thick SiO₂/Si substrate was located with OM measurement. Then, the sample was loaded into a focused ion beam (FIB)-scanning electron microscopy (SEM) chamber operated with ultrahigh vacuum. Then, 30 nm followed by 2 μ m thick Pt was carefully deposited onto the sample. The lamellar sample on the substrate was transferred to a copper TEM grid as a side-on configuration via a needle for the subsequent measurement (see Figure S4A–C for sample preparation).

ASSOCIATED CONTENT

Supporting Information

The Supporting Information is available free of charge at <https://pubs.acs.org/doi/10.1021/acsami.2c12592>.

Discussion of solvatochromism and compressive stain on TMDC/hBN/SC; full explanation of EFM; effect of each constituent for TMDC dispersions (Figure S1); extinction spectra of spectrum valley-normalized TMDC/hBN/SC dispersions (Figure S2); stability of TMDC/hBN/SC dispersion over time (Figure S3); preparation of the cross-sectional TEM sample via FIB-SEM (Figure S4); cross-sectional TEM measurement of MoS₂/hBN on the 285 nm thick SiO₂/Si substrate (Figure S5); effect of each constituent for MoS₂, WSe₂, and MoSe₂-related dispersions (Figure S6); and interlayer coupling, photoluminescence, and overtones between TMDC and hBN (Figure S7) (PDF)

AUTHOR INFORMATION

Corresponding Authors

Eunji Lee – School of Materials Science and Engineering, Gwangju Institute of Science and Technology, Gwangju 61005, Republic of Korea; orcid.org/0000-0001-7494-1776; Email: eunjilee@gist.ac.kr

Sang-Yong Ju – Department of Chemistry, Yonsei University, Seoul 03722, Republic of Korea; orcid.org/0000-0002-6939-5296; Email: syju@yonsei.ac.kr

Authors

Junmo Park – Department of Chemistry, Yonsei University, Seoul 03722, Republic of Korea; orcid.org/0000-0003-4217-9056

Sungmin Bong – Department of Chemistry, Yonsei University, Seoul 03722, Republic of Korea

Jaehyun Park – School of Materials Science and Engineering, Gwangju Institute of Science and Technology, Gwangju 61005, Republic of Korea

Complete contact information is available at: <https://pubs.acs.org/doi/10.1021/acsami.2c12592>

Author Contributions

[§]J.P. and S.B. contributed equally. S.-Y.J. conceived the idea and wrote the manuscript. J.P. and S.B. performed the experiments. J.P. and E.L. conducted the TEM experiment. All of the images/artwork/photographs that appear in the manuscript and SI file, including those in the TOC graphic, were created by the authors of this manuscript.

Notes

The authors declare no competing financial interest.

ACKNOWLEDGMENTS

This research was supported financially by the Basic Science Research Program (2020R1F1A1076983 and 2020R1A4A1017737) and Technology Development Program to Solve Climate Changes (2020M1A2A2080748) through the National Research Foundation of Korea (NRF) funded by the Ministry of Education, Science, and Technology.

REFERENCES

- (1) Kang, J.; Tongay, S.; Zhou, J.; Li, J.; Wu, J. Band Offsets and Heterostructures of Two-Dimensional Semiconductors. *Appl. Phys. Lett.* **2013**, *102*, No. 012111.
- (2) Splendiani, A.; Sun, L.; Zhang, Y.; Li, T.; Kim, J.; Chim, C.-Y.; Galli, G.; Wang, F. Emerging Photoluminescence in Monolayer MoS₂. *Nano Lett.* **2010**, *10*, 1271–1275.
- (3) Radisavljevic, B.; Radenovic, A.; Brivio, J.; Giacometti, V.; Kis, A. Single-Layer MoS₂ Transistors. *Nat. Nanotechnol.* **2011**, *6*, 147–150.
- (4) Lee, H. S.; Shin, J. M.; Jeon, P. J.; Lee, J.; Kim, J. S.; Hwang, H. C.; Park, E.; Yoon, W.; Ju, S.-Y.; Im, S. Few-Layer MoS₂–Organic Thin-Film Hybrid Complementary Inverter Pixel Fabricated on a Glass Substrate. *Small* **2015**, *11*, 2132–2138.
- (5) Choi, K.; Raza, S. R. A.; Lee, H. S.; Jeon, P. J.; Pezeshki, A.; Min, S.-W.; Kim, J. S.; Yoon, W.; Ju, S.-Y.; Lee, K.; Im, S. Trap Density Probing on Top-Gate MoS₂ Nanosheet Field-Effect Transistors by Photo-Excited Charge Collection Spectroscopy. *Nanoscale* **2015**, *7*, 5617–5623.
- (6) Lee, G.-H.; Yu, Y.-J.; Cui, X.; Petrone, N.; Lee, C.-H.; Choi, M. S.; Lee, D.-Y.; Lee, C.; Yoo, W. J.; Watanabe, K.; Taniguchi, T.; Nuckolls, C.; Kim, P.; Hone, J. Flexible and Transparent MoS₂ Field-Effect Transistors on Hexagonal Boron Nitride-Graphene Heterostructures. *ACS Nano* **2013**, *7*, 7931–7936.
- (7) Ye, G.; Gong, Y.; Lin, J.; Li, B.; He, Y.; Pantelides, S. T.; Zhou, W.; Vajtai, R.; Ajayan, P. M. Defects Engineered Monolayer MoS₂ for Improved Hydrogen Evolution Reaction. *Nano Lett.* **2016**, *16*, 1097–1103.
- (8) Lee, Y.-H.; Zhang, X.-Q.; Zhang, W.; Chang, M.-T.; Lin, C.-T.; Chang, K.-D.; Yu, Y.-C.; Wang, J. T.-W.; Chang, C.-S.; Li, L.-J.; Lin, T.-W. Synthesis of Large-Area MoS₂ Atomic Layers with Chemical Vapor Deposition. *Adv. Mater.* **2012**, *24*, 2320–2325.
- (9) Mak, K. F.; He, K.; Shan, J.; Heinz, T. F. Control of Valley Polarization in Monolayer MoS₂ by Optical Helicity. *Nat. Nanotechnol.* **2012**, *7*, 494–498.
- (10) Coleman, J. N.; Lotya, M.; O'Neill, A.; Bergin, S. D.; King, P. J.; Khan, U.; Young, K.; Gaucher, A.; De, S.; Smith, R. J.; Shvets, I. V.; Arora, S. K.; Stanton, G.; Kim, H.-Y.; Lee, K.; Kim, G. T.; Duesberg, G. S.; Hallam, T.; Boland, J. J.; Wang, J. J.; Donegan, J. F.; Grunlan, J. C.; Moriarty, G.; Shmeliov, A.; Nicholls, R. J.; Perkins, J. M.; Grievson, E. M.; Theuwissen, K.; McComb, D. W.; Nellist, P. D.; Nicolosi, V. Two-Dimensional Nanosheets Produced by Liquid Exfoliation of Layered Materials. *Science* **2011**, *331*, 568–571.
- (11) Smith, R. J.; King, P. J.; Lotya, M.; Wirtz, C.; Khan, U.; De, S.; O'Neill, A.; Duesberg, G. S.; Grunlan, J. C.; Moriarty, G.; Chen, J.; Wang, J.; Minett, A. I.; Nicolosi, V.; Coleman, J. N. Large-Scale Exfoliation of Inorganic Layered Compounds in Aqueous Surfactant Solutions. *Adv. Mater.* **2011**, *23*, 3944–3948.
- (12) Eda, G.; Yamaguchi, H.; Vohry, D.; Fujita, T.; Chen, M.; Chhowalla, M. Photoluminescence from Chemically Exfoliated MoS₂. *Nano Lett.* **2011**, *11*, 5111–5116.
- (13) Zheng, J.; Zhang, H.; Dong, S.; Liu, Y.; Tai Nai, C.; Suk Shin, H.; Young Jeong, H.; Liu, B.; Ping Loh, K. High Yield Exfoliation of Two-Dimensional Chalcogenides Using Sodium Naphthalenide. *Nat. Commun.* **2014**, *5*, No. 2995.
- (14) Zeng, Z.; Yin, Z.; Huang, X.; Li, H.; He, Q.; Lu, G.; Boey, F.; Zhang, H. Single-Layer Semiconducting Nanosheets: High-Yield Preparation and Device Fabrication. *Angew. Chem., Int. Ed.* **2011**, *50*, 11093–11097.
- (15) Yang, R.; Mei, L.; Zhang, Q.; Fan, Y.; Shin, H. S.; Vohry, D.; Zeng, Z. High-Yield Production of Mono- or Few-layer Transition Metal Dichalcogenide Nanosheets by an Electrochemical Lithium Ion Intercalation-Based Exfoliation Method. *Nat. Protoc.* **2022**, *17*, 358–377.
- (16) Chou, S. S.; De, M.; Kim, J.; Byun, S.; Dykstra, C.; Yu, J.; Huang, J.; Dravid, V. P. Ligand Conjugation of Chemically Exfoliated MoS₂. *J. Am. Chem. Soc.* **2013**, *135*, 4584–4587.
- (17) Jeong, M.; Kim, S.; Ju, S.-Y. Preparation and Characterization of a Covalent Edge-Functionalized Lipoic Acid–MoS₂ Conjugate. *RSC Adv.* **2016**, *6*, 36248–36255.
- (18) Griffin, A.; Nisi, K.; Pepper, J.; Harvey, A.; Szydłowska, B. M.; Coleman, J. N.; Backes, C. Effect of Surfactant Choice and Concentration on the Dimensions and Yield of Liquid-Phase-Exfoliated Nanosheets. *Chem. Mater.* **2020**, *32*, 2852–2862.

- (19) Backes, C.; Smith, R. J.; McEvoy, N.; Berner, N. C.; McCloskey, D.; Nerl, H. C.; O'Neill, A.; King, P. J.; Higgins, T.; Hanlon, D.; Scheuschner, N.; Maultzsch, J.; Houben, L.; Duesberg, G. S.; Donegan, J. F.; Nicolosi, V.; Coleman, J. N. Edge and Confinement Effects Allow in situ Measurement of Size and Thickness of Liquid-Exfoliated Nanosheets. *Nat. Commun.* **2014**, *5*, No. 4576.
- (20) Mei, L.; Gao, X.; Gao, Z.; Zhang, Q.; Yu, X.; Rogach, A. L.; Zeng, Z. Size-Selective Synthesis of Platinum Nanoparticles on Transition-Metal Dichalcogenides for the Hydrogen Evolution Reaction. *Chem. Commun.* **2021**, *57*, 2879–2882.
- (21) Blase, X.; Rubio, A.; Louie, S. G.; Cohen, M. L. Quasiparticle Band Structure of Bulk Hexagonal Boron Nitride and Related Systems. *Phys. Rev. B* **1995**, *51*, 6868–6875.
- (22) Kostoglou, N.; Polychronopoulou, K.; Rebholz, C. Thermal and Chemical Stability of Hexagonal Boron Nitride (h-BN) Nanoplatelets. *Vacuum* **2015**, *112*, 42–45.
- (23) Lin, Y.; Connell, J. W. Advances in 2D Boron Nitride Nanostructures: Nanosheets, Nanoribbons, Nanomeshes, and Hybrids with Graphene. *Nanoscale* **2012**, *4*, 6908–6939.
- (24) Golberg, D.; Bando, Y.; Huang, Y.; Terao, T.; Mitome, M.; Tang, C.; Zhi, C. Boron Nitride Nanotubes and Nanosheets. *ACS Nano* **2010**, *4*, 2979–2993.
- (25) Khan, A. F.; Down, M. P.; Smith, G. C.; Foster, C. W.; Banks, C. E. Surfactant-Exfoliated 2D Hexagonal Boron Nitride (2D-hBN): Role of Surfactant upon the Electrochemical Reduction of Oxygen and Capacitance Applications. *J. Mater. Chem. A* **2017**, *5*, 4103–4113.
- (26) Shi, X.; Wang, K.; Tian, J.; Yin, X.; Guo, B.; Xi, G.; Wang, W.; Wu, W. Few-Layer Hydroxyl-Functionalized Boron Nitride Nanosheets for Nanoscale Thermal Management. *ACS Appl. Nano Mater.* **2020**, *3*, 2310–2321.
- (27) Santhanalakshmi, J.; Lakshmi, G. S.; Aswal, V. K.; Goyal, P. S. Small-Angle Neutron Scattering Study of Sodium Cholate and Sodium Deoxycholate Interacting Micelles in Aqueous Medium. *J. Chem. Sci.* **2001**, *113*, 55–62.
- (28) Han, X.; Lin, J.; Liu, J.; Wang, N.; Pan, D. Effects of Hexagonal Boron Nitride Encapsulation on the Electronic Structure of Few-Layer MoS₂. *J. Phys. Chem. C* **2019**, *123*, 14797–14802.
- (29) Zhou, K.-G.; Withers, F.; Cao, Y.; Hu, S.; Yu, G.; Casiraghi, C. Raman Modes of MoS₂ Used as Fingerprint of van der Waals Interactions in 2-D Crystal-Based Heterostructures. *ACS Nano* **2014**, *8*, 9914–9924.
- (30) Bogdanova, L. R.; Gnezdilov, O. I.; Idiyatullin, B. Z.; Kurbanov, R. K.; Zuev, Y. F.; Us'yarov, O. G. Micellization in Sodium Deoxycholate Solutions. *Colloid J.* **2012**, *74*, 1–6.
- (31) Pártay, L. B.; Jedlovsky, P.; Sega, M. Molecular Aggregates in Aqueous Solutions of Bile Acid Salts. Molecular Dynamics Simulation Study. *J. Phys. Chem. B* **2007**, *111*, 9886–9896.
- (32) Kozawa, D.; Kumar, R.; Carvalho, A.; Kumar Amara, K.; Zhao, W.; Wang, S.; Toh, M.; Ribeiro, R. M.; Castro Neto, A. H.; Matsuda, K.; Eda, G. Photocarrier Relaxation Pathway in Two-Dimensional Semiconducting Transition Metal Dichalcogenides. *Nat. Commun.* **2014**, *5*, No. 4543.
- (33) Dias, A. C.; Qu, F.; Azevedo, D. L.; Fu, J. Band Structure of Monolayer Transition-Metal Dichalcogenides and Topological Properties of Their Nanoribbons: Next-Nearest-Neighbor Hopping. *Phys. Rev. B* **2018**, *98*, No. 075202.
- (34) Beal, A. R.; Knights, J. C.; Liang, W. Y. Transmission Spectra of Some Transition Metal Dichalcogenides. II. Group VIA: Trigonal Prismatic Coordination. *J. Phys. C: Solid State* **1972**, *5*, 3540–3551.
- (35) Zhao, W.; Ghorannevis, Z.; Amara, K. K.; Pang, J. R.; Toh, M.; Zhang, X.; Kloc, C.; Tan, P. H.; Eda, G. Lattice Dynamics in Mono- and Few-Layer Sheets of WS₂ and WSe₂. *Nanoscale* **2013**, *5*, 9677–9683.
- (36) Mao, N.; Chen, Y.; Liu, D.; Zhang, J.; Xie, L. Solvatochromic Effect on the Photoluminescence of MoS₂ Monolayers. *Small* **2013**, *9*, 1312–1315.
- (37) Laturia, A.; Van de Put, M. L.; Vandenberghe, W. G. Dielectric Properties of Hexagonal Boron Nitride and Transition Metal Dichalcogenides: from Monolayer to Bulk. *npj 2D Mater. Appl.* **2018**, *2*, No. 6.
- (38) Bockrath, M.; Markovic, N.; Shepard, A.; Tinkham, M.; Gurevich, L.; Kouwenhoven, L. P.; Wu, M. W.; Sohn, L. L. Scanned Conductance Microscopy of Carbon Nanotubes and λ -DNA. *Nano Lett.* **2002**, *2*, 187–190.
- (39) Park, J.; Han, Y. R.; Park, M.; Jun, C.-H.; Ju, S.-Y. Coral Reef-Like Functionalized Self-Assembled Monolayers for Network Formation of Carbon Nanotube with Diameter Selectivity. *Carbon* **2020**, *161*, 599–611.
- (40) Shang, J.; Xue, F.; Fan, C.; Ding, E. Preparation of Few Layers Hexagonal Boron Nitride Nanosheets via High-Pressure Homogenization. *Mater. Lett.* **2016**, *181*, 144–147.
- (41) Geick, R.; Perry, C. H.; Rupprecht, G. Normal Modes in Hexagonal Boron Nitride. *Phys. Rev.* **1966**, *146*, 543–547.
- (42) Hunter, R. J. Chapter 2 - Charge and Potential Distribution at Interfaces. In *Zeta Potential in Colloid Science*; Hunter, R. J., Ed.; Academic Press, 1981; pp 11–58.
- (43) Berkdemir, A.; Gutiérrez, H. R.; Botello-Méndez, A. R.; Perea-López, N.; Elías, A. L.; Chia, C.-I.; Wang, B.; Crespi, V. H.; López-Urías, F.; Charlier, J.-C.; Terrones, H.; Terrones, M. Identification of Individual and Few Layers of WS₂ Using Raman Spectroscopy. *Sci. Rep.* **2013**, *3*, No. 1755.
- (44) Pak, S.; Lee, J.; Lee, Y.-W.; Jang, A. R.; Ahn, S.; Ma, K. Y.; Cho, Y.; Hong, J.; Lee, S.; Jeong, H. Y.; Im, H.; Shin, H. S.; Morris, S. M.; Cha, S.; Sohn, J. I.; Kim, J. M. Strain-Mediated Interlayer Coupling Effects on the Excitonic Behaviors in an Epitaxially Grown MoS₂/WS₂ van der Waals Heterobilayer. *Nano Lett.* **2017**, *17*, 5634–5640.
- (45) Lee, C.; Jeong, B. G.; Yun, S. J.; Lee, Y. H.; Lee, S. M.; Jeong, M. S. Unveiling Defect-Related Raman Mode of Monolayer WS₂ via Tip-Enhanced Resonance Raman Scattering. *ACS Nano* **2018**, *12*, 9982–9990.
- (46) Sahin, H.; Tongay, S.; Horzum, S.; Fan, W.; Zhou, J.; Li, J.; Wu, J.; Peeters, F. M. Anomalous Raman Spectra and Thickness-Dependent Electronic Properties of WSe₂. *Phys. Rev. B* **2013**, *87*, No. 165409.
- (47) Jin, C.; Kim, J.; Suh, J.; Shi, Z.; Chen, B.; Fan, X.; Kam, M.; Watanabe, K.; Taniguchi, T.; Tongay, S.; Zettl, A.; Wu, J.; Wang, F. Interlayer Electron-Phonon Coupling in WSe₂/hBN Heterostructures. *Nat. Phys.* **2017**, *13*, 127–131.
- (48) Hauner, I. M.; Deblais, A.; Beattie, J. K.; Kellay, H.; Bonn, D. The Dynamic Surface Tension of Water. *J. Phys. Chem. Lett.* **2017**, *8*, 1599–1603.
- (49) Govind Rajan, A.; Strano, M. S.; Blankschtein, D. Liquids with Lower Wettability Can Exhibit Higher Friction on Hexagonal Boron Nitride: The Intriguing Role of Solid-Liquid Electrostatic Interactions. *Nano Lett.* **2019**, *19*, 1539–1551.
- (50) Gaur, A. P. S.; Sahoo, S.; Ahmadi, M.; Dash, S. P.; Guinel, M. J. F.; Katiyar, R. S. Surface Energy Engineering for Tunable Wettability through Controlled Synthesis of MoS₂. *Nano Lett.* **2014**, *14*, 4314–4321.
- (51) Annamalai, M.; Gopinadhan, K.; Han, S. A.; Saha, S.; Park, H. J.; Cho, E. B.; Kumar, B.; Patra, A.; Kim, S.-W.; Venkatesan, T. Surface Energy and Wettability of van der Waals Structures. *Nanoscale* **2016**, *8*, 5764–5770.
- (52) Koo, E.; Ju, S.-Y. Role of Residual Polymer on Chemical Vapor Grown Graphene by Raman Spectroscopy. *Carbon* **2015**, *86*, 318–324.
- (53) Koo, E.; Kim, S.; Ju, S.-Y. Relationships between the Optical and Raman Behavior of van Hove Singularity in Twisted Bi- and Fewlayer Graphenes and Environmental Effects. *Carbon* **2017**, *111*, 238–247.
- (54) Koo, E.; Lee, Y.; Song, Y.; Park, M.; Ju, S.-Y. Growth Order-Dependent Strain Variations of Lateral Transition Metal Dichalcogenide Heterostructures. *ACS Appl. Electron. Mater.* **2019**, *1*, 113–121.
- (55) Song, Y.; Park, M.; Park, J.; Ahn, H. S.; Kim, T. K.; Ju, S.-Y. Long-Term Exposure of MoS₂ to Oxygen and Water Promoted Armchair-to-Zigzag-Directional Line Unzippings. *Nanomaterials* **2022**, *12*, No. 1706.

Hierarchical Van Der Waals Heterostructure Strategy to Form Stable Transition Metal Dichalcogenide Dispersions

*Junmo Park,^{†, §} Sungmin Bong,^{†, §} Jaehyun Park,[‡] Eunji Lee,^{‡, *} and Sang-Yong Ju^{†, *}*

[†]Department of Chemistry, Yonsei University, 50 Yonsei-ro, Seodaemun-Gu, Seoul 03722, Republic of Korea; [‡]School of Materials Science and Engineering, Gwangju Institute of Science and Technology,

123 Cheomdangwagi-ro, Buk-gu, Gwangju 61005, Republic of Korea

[§] Equally contributed to this work.

* Correspondence E-mail: eunjilee@gist.ac.kr (Eunji Lee); syju@yonsei.ac.kr (Sang-Yong Ju)

Table of Contents	S1
Discussion of solvatochromism and compressive stain on TMDC/hBN/SC	S2
Full explanation of EFM	S3
Figure S1. Effect of each constituent for TMDC dispersions	S4
Figure S2. Extinction spectra of spectrum valley-normalized TMDC/hBN/SC dispersions	S4
Figure S3. Stability of TMDC/hBN/SC dispersion over time	S5
Figure S4. Preparation of cross-sectional TEM sample <i>via</i> FIB-SEM	S5
Figure S5. Cross-sectional TEM measurement of MoS ₂ /hBN on 285 nm-thick SiO ₂ /Si substrate	S6
Figure S6. Effect of each constituent for MoS ₂ -, WSe ₂ -, and MoSe ₂ -related dispersions	S7
Figure S7. Interlayer coupling, photoluminescence and overtones between TMDC and hBN observed in Raman spectra	S7
Cited reference	S8

Discussion of solvatochromism and compressive strain on TMDC/hBCB/SC:

The progressive blueshift is likely to be related to strain associated with hBN. For instance, MoS₂/hBN/SC exhibit progressive blueshift of A transition up to 654 nm (or 1.896 eV). Solvatochromism of monolayer MoS₂ upon contact with *n*-hexane (dielectric constant (ϵ): 1.89) induces 1.836 eV except solvents promoting *n*- or *p*-dopings¹, which is not the case of hBN. A consideration of the ϵ of monolayer hBN (3.29 and 6.82 for static out-of-plane and in-plane ϵ 's, respectively)¹ suggests that the aforementioned solvatochromism² is not the main source of the observed blueshifts of the TMDC/hBN/SC dispersions. These findings indicate that hBN rather than SC is in intimate contact with TMDC and plays an important role in governing the positions of optical transitions. Therefore, hBN wrapped around the TMDC against external water might exert strain on the TMDC that results in blueshifts or redshifts in excitonic bands.³ For instance, monolayer MoS₂ and MoSe₂ exhibit respective A position shifts with respective 99 and 90 meV/ % as a result of compressive biaxial strain.^{3, 4} A comparison of the A position shift suggests that MoS₂ and MoSe₂ experience respective 0.17 % and 0.20 % biaxial compressive strain at centrifugation levels of 1 kg to 12 kg. In the cases of WS₂ and WSe₂, only uniaxial strain promoted exciton shift data have been reported (WS₂: 50 meV/ %, WSe₂: 49 meV/ %).⁵ Since the optical shift response associated with biaxial strain is about twice as much as that of uniaxial strain,⁶ the respective biaxial strain of WS₂/hBN/SC and WSe₂/hBN/SC are estimated to be 100 and 98 meV/ %, respectively. Thus, increasing centrifugal force from 1 to 12 kg increases compressive biaxial strain by 0.17-0.29 %, respectively. The excitonic position shifts do not occur in spectra of TMDC dispersion prepared only using SC.⁷ It is interesting that hBN not only encapsulates TMDC in water as described in Figure 1A, it exerts compressive strain on the TMDC by mainly squeezing it laterally. Possibly, a portion of the compressive strain arises from wrinkles formed between TMDC/hBN due to the strong vdW interaction.⁸

Full explanation of EFM:

Dual frequency EFM is shown in Figure 4A. The additional lock-in amplifier for the EFM signal is embedded in the AFM controller and serves two purposes: first, in addition to the DC bias, the application of the AC voltage with the tip frequency ω . The second is the separation of the signal component at ω , which carries the EFM data, from the topography signal detected at the cantilever resonance ω_0 . In the dual frequency EFM, the tip and the sample can be viewed as a capacitor, ω from the topography signal detected at the cantilever resonance ω_0 . In the dual frequency EFM, the tip and the sample can be viewed as a capacitor, with an oscillating electrostatic interaction force F_{el} given as:

$$F_{el} = \frac{1\partial C}{2\partial d}V^2 \quad (S1)$$

With tip-sample capacitance C in a distance d and the total voltage V . Since both AC and DC voltages are applied simultaneously between the tip and the sample, the total voltage V between the tip and the sample is expressed by the following equation:

$$V(t) = V_T - V_S + V_{AC}\sin\omega_{tip}t \quad (S2)$$

Where V_T is the DC tip bias, V_S is the surface potential on the sample and V_{AC} and ω_{tip} are the amplitude and frequency of the applied AC voltage, respectively. The combination of the above equations results in three terms that describe the electrostatic force:

$$F_{el} = \frac{1\partial C}{2\partial d}V(t)^2 \quad (S3)$$

$$= \frac{1\partial C}{2\partial d}\left[(V_T - V_S)^2 + \frac{1}{2}V_{AC}^2\right] + \frac{\partial C}{\partial d}[(V_T - V_S)(V_{AC}\sin\omega_{tip}t)] - \frac{1\partial C}{4\partial d}[(V_{AC}^2\cos 2\omega_{tip}t)]$$

These terms can be referred to as static DC term, and two AC terms at ω_{tip} and $2\omega_{tip}$. Whereas the static DC term is difficult to detect, the second lock-in amplifier used for EFM can accurately decouple the AC term at ω_{tip} to image the electrostatic properties of the sample. The amplitude at ω_{tip} contains information on the magnitude of the electrostatic charging of the sample, while the phase contains information on the sign of the surface charge.

Figure S1. Effect of each constituent for TMDC dispersions. Extinction spectrum changes of (A) WS_2 , (B) MoS_2 , (C) WSe_2 , and (D) MoSe_2 with increasing centrifugal force.

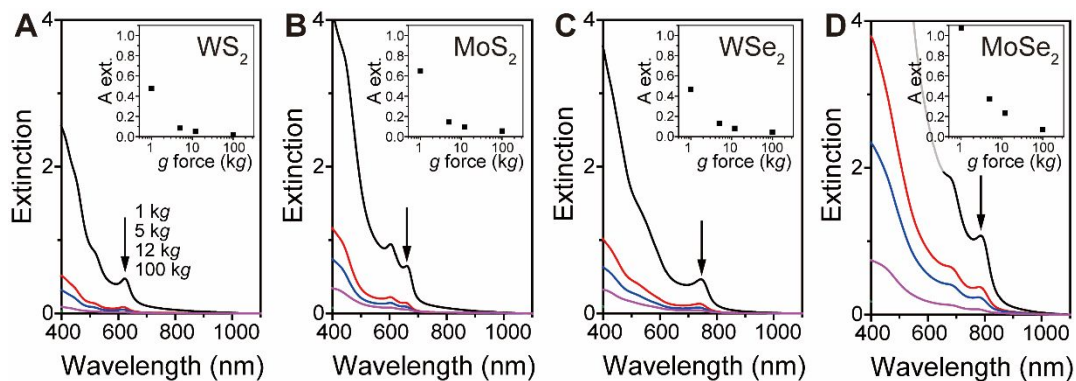


Figure S2. Extinction spectra of spectrum valley-normalized TMDC/hBN/SC dispersions.

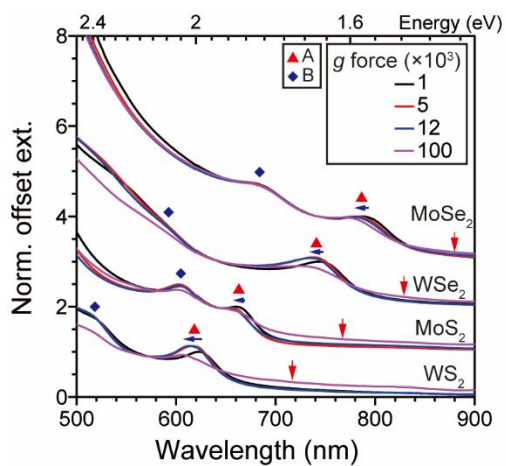


Figure S3. Stability of TMDC/hBN/SC dispersion over time. The offset extinction spectra of (red) as-dispersed and (black) three years-old sample from 12 kg centrifugation. (B) the percentile ratio of extinction of A from as-dispersed ($Ext_{A,as-dispersed}$) over extinction of A from the aged sample ($Ext_{A,aged}$) according to TMDC and g forces. (C) A transition shifts according to TMDC and g forces.

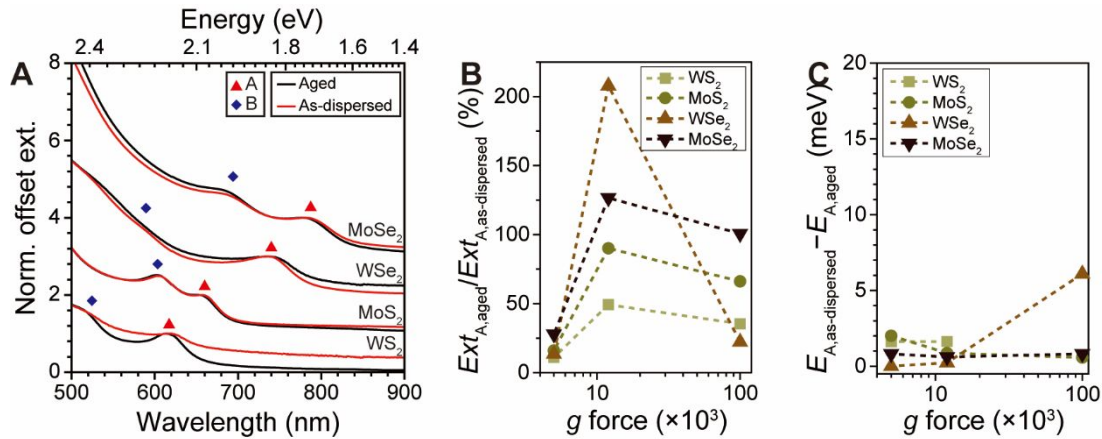


Figure S4. Preparation of cross-sectional TEM sample *via* FIB-SEM. (A) OM image of target sample. (B) Pit formation around Pt-coated sample by FIB milling in FIB-SEM. Samples are “dam”-like lamellar structure in which lamellar structure is not visible. (C) Mounting the lamellar sample on tooth of TEM grid. Pt/sample/SiO₂/Si cross-section is visible. Inset: TEM grid for measurement.

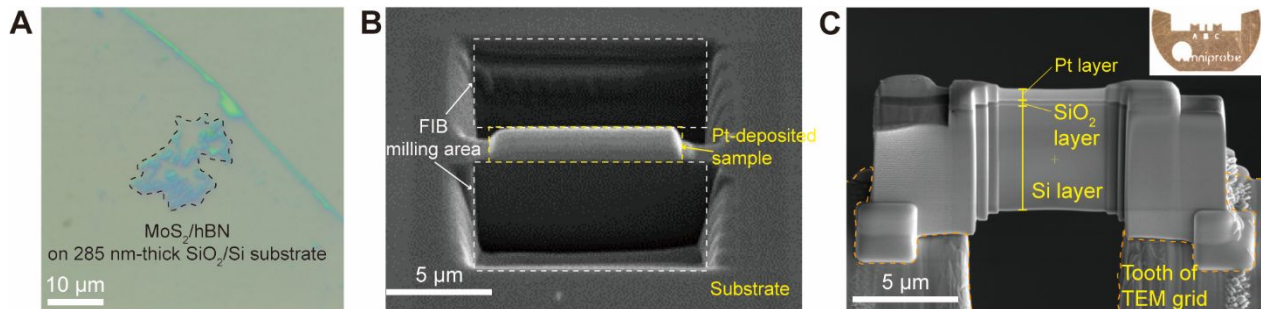


Figure S5. Cross-sectional TEM measurement of MoS₂/hBN on 285 nm-thick SiO₂/Si substrate. (A) TEM image of hierarchical hBN/MoS₂/SiO₂. (B) Whole image and (C) energy-dispersive images of B, N, Mo, and S by EDS measurement. The reason for broad distribution of B image originates from lower binding energy of boron K edge close to background. (D–F) Similar measurements of other MoS₂/hBN area.

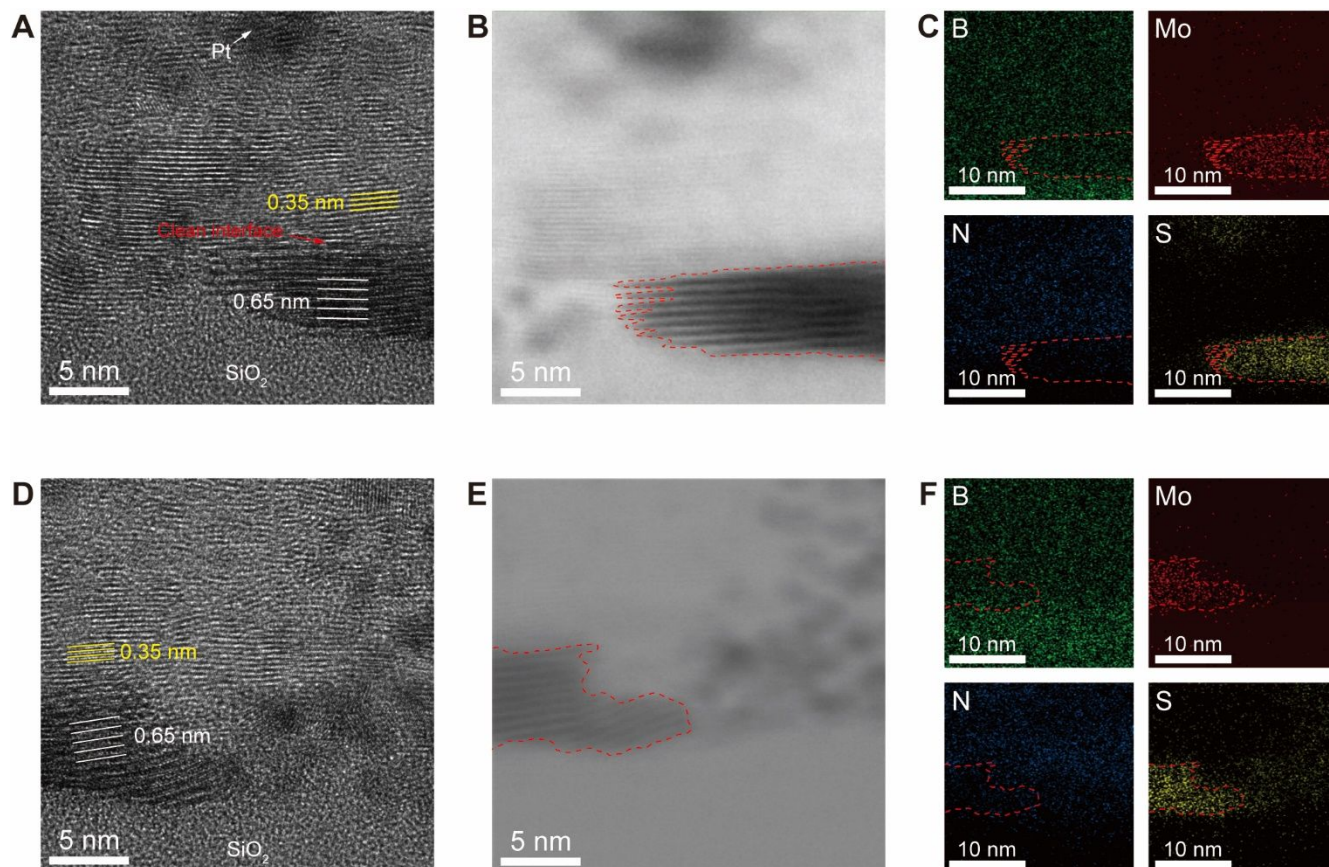


Figure S6. Effect of each constituent for MoS₂-, WSe₂-, and MoSe₂-related dispersions. Normalized extinction spectra of (A) MoS₂-, (B) WSe₂- and (C) MoSe₂-related dispersions.

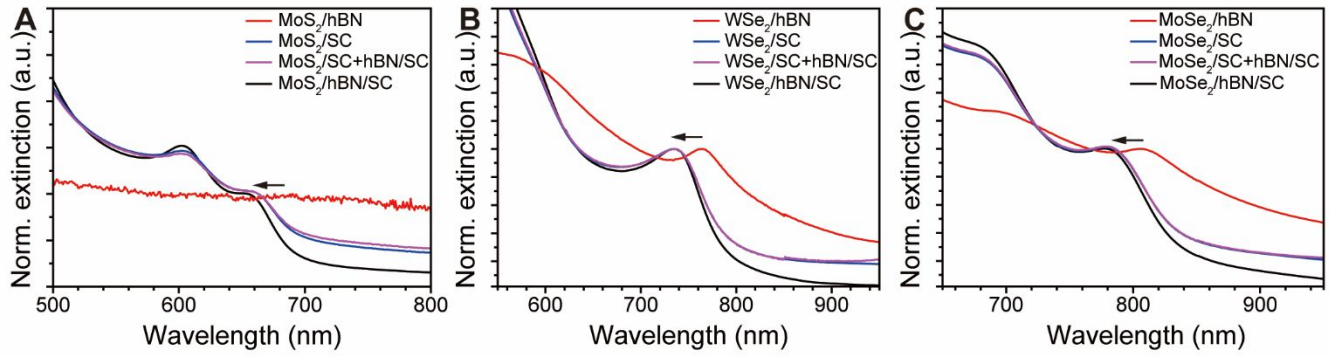
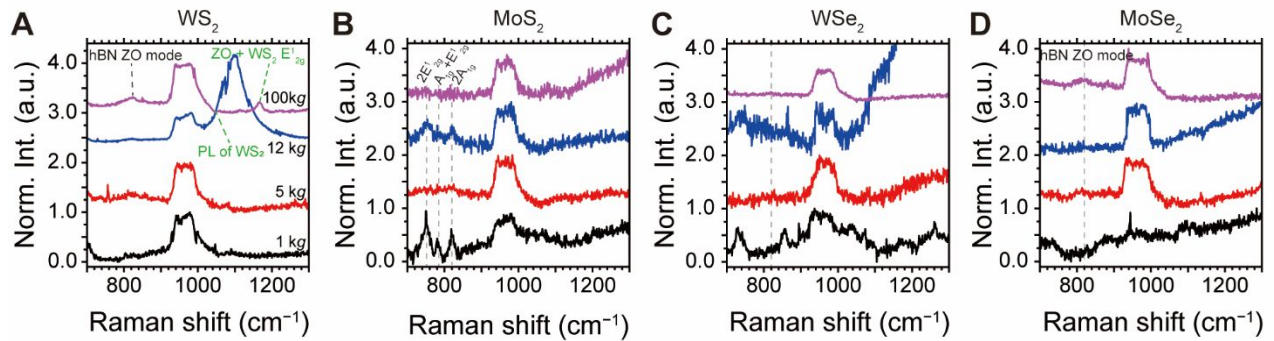


Figure S7. (A-D) Interlayer coupling, photoluminescence and overtones between TMDC and hBN from TMDC/hBN/SC dispersions observed in Raman spectra.



Cited reference

1. Laturia, A.; Van de Put, M. L.; Vandenberghe, W. G., Dielectric Properties of Hexagonal Boron Nitride and Transition Metal Dichalcogenides: from Monolayer to Bulk. *npj 2D Mater. Appl.* **2018**, *2* (1), 6.
2. Mao, N.; Chen, Y.; Liu, D.; Zhang, J.; Xie, L., Solvatochromic Effect on the Photoluminescence of MoS₂ Monolayers. *Small* **2013**, *9* (8), 1312-1315.
3. Lloyd, D.; Liu, X.; Christopher, J. W.; Cantley, L.; Wadehra, A.; Kim, B. L.; Goldberg, B. B.; Swan, A. K.; Bunch, J. S., Band Gap Engineering with Ultralarge Biaxial Strains in Suspended Monolayer MoS₂. *Nano Lett.* **2016**, *16* (9), 5836-5841.
4. Frisenda, R.; Drüppel, M.; Schmidt, R.; Michaelis de Vasconcellos, S.; Perez de Lara, D.; Bratschitsch, R.; Rohlfing, M.; Castellanos-Gomez, A., Biaxial Strain Tuning of the Optical Properties of Single-Layer Transition Metal Dichalcogenides. *npj 2D Mater. Appl.* **2017**, *1* (1), 10.
5. Niehues, I.; Schmidt, R.; Drüppel, M.; Marauhn, P.; Christiansen, D.; Selig, M.; Berghäuser, G.; Wigger, D.; Schneider, R.; Braasch, L.; Koch, R.; Castellanos-Gomez, A.; Kuhn, T.; Knorr, A.; Malic, E.; Rohlfing, M.; Michaelis de Vasconcellos, S.; Bratschitsch, R., Strain Control of Exciton–Phonon Coupling in Atomically Thin Semiconductors. *Nano Lett.* **2018**, *18* (3), 1751-1757.
6. Carrascoso, F.; Frisenda, R.; Castellanos-Gomez, A., Biaxial Versus Uniaxial Strain Tuning of Single-Layer MoS₂. *Nano Mater. Sci.* **2022**, *4* (1), 44-51.
7. Griffin, A.; Nisi, K.; Pepper, J.; Harvey, A.; Szydłowska, B. M.; Coleman, J. N.; Backes, C., Effect of Surfactant Choice and Concentration on the Dimensions and Yield of Liquid-Phase-Exfoliated Nanosheets. *Chem. Mater.* **2020**, *32* (7), 2852-2862.
8. Ares, P.; Wang, Y. B.; Woods, C. R.; Dougherty, J.; Fumagalli, L.; Guinea, F.; Davidovitch, B.; Novoselov, K. S., Van der Waals Interaction Affects Wrinkle Formation in Two-Dimensional Materials. *Proc. Nat. Acad. Sci.* **2021**, *118* (14), e2025870118.

